Thin and Subvisual Tropopause Tropical Cirrus: Observations and Radiative Impacts

GREG M. MCFARQUHAR AND ANDREW J. HEYMSFIELD

National Center for Atmospheric Research, Boulder, Colorado*

JAMES SPINHIRNE AND BILL HART

NASA Goddard Space Research Center, Greenbelt, Maryland

(Manuscript received 29 January 1999, in final form 6 August 1999)

ABSTRACT

In situ microphysical, remote sensing, and satellite observations of thin and subvisible cirrus have been used to establish their frequency of occurrence, determine their mean optical depths and radiative forcings, and to analyze their association with deep convection. A spatially thin layer of cirrus, with both base and top above 15 km, was observed in the central Pacific Tropics 29% of the time, with a mean thickness of 0.47 km, using a nadir-pointing Nd:YAG lidar operating at 1.064 μm during the Central Equatorial Pacific Experiment (CEPEX). In situ microphysical data collected in the mid-1970s and mid-1980s by a WB-57 and Learjet near Kwajalein, Marshall Islands, are revisited to determine typical ice crystal sizes and shapes that occur in this cloud type. Three observed vertical profiles, obtained from ascents/descents through cloud, are used with a δ-four-stream radiative transfer model to calculate observed heating rates of up to 1.0 K day^{-1}, principally in the infrared, and cloud radiative forcings of up to 1.2 W m^{-2}. These calculations are extended using remotely sensed optical depths acquired with the airborne lidar on four days during CEPEX; the average τ estimated was 0.01, and the corresponding heating rates and cloud radiative forcings were 1.66 K day^{-1} and 1.6 W m^{-2}, respectively. Using a visibility threshold for τ of 0.03, this suggests that the majority of the thin cirrus observed are subvisible. The calculated radiative effects depend principally on the observed optical thickness of the cloud layers.

Altitude-dependent average extinction coefficients between 0.001 and 0.004 km^{-1} were calculated from the limb-viewing Stratospheric Aerosol and Gas Experiment (SAGE) II satellite, confirming that the lidar estimated τ is representative for the Tropics. A comparison of the SAGE II observed occurrence times with cloud properties estimated from collocated International Satellite Cloud and Climatology Project retrievals for the closest time shows that 28% of the subvisible cirrus occurred within the same 2.5° by 2.5° grid box as deep convection.

Although the effect of subvisible cirrus on the radiative budget of the Tropics is not as large as for other ice clouds, their effects are not negligible and their other impacts, such as enhancing upper-tropospheric vertical motions and the lower-stratospheric water vapor, should not be ignored.

1. Introduction

During the Central Equatorial Pacific Experiment (CEPEX) and the Tropical Ocean Global Atmosphere Coupled Ocean–Atmosphere Response Experiment (TOGA COARE), a geometrically thin layer of cirrus was frequently observed near the tropopause by Spinhirne, using his cloud lidar system (CLS) (Spinhirne et al. 1996) on board the NASA ER-2, which overflew cloud systems at 19-km altitude. Prabhakara et al. (1993), using *Nimbus-4* Infrared Interferometer Spectrometer (IRIS) measurements, and Wang et al. (1994), using the Stratospheric Aerosol Gas Experiment (SAGE) II measurements, both observed optically thin cirrus near the tropopause more than 50% of the time in warm pool regions. Using ground-based lidar, Uthe and Russell (1977) also established a high frequency of occurrence of subvisible cirrus that typically persisted for several days. More recently, Nee et al. (1998) found subvisible cirrus with average geometrical and optical thicknesses of 0.6 and 0.008 km, respectively, occurring approximately 50% of the time using a lidar operating at Chang-Li, Taiwan, at 25°N. Platt et al. (1998) also detected subvisible cirrus with visible and infrared optical depths as low as 0.01 in Kavieng, Papua, New Guinea, at 3°S in 1993 using a lidar. From near-global observations of optically thin cirrus during the Lidar Inspace Technology Experiment, Winker and Trepte (1998) found layers of cirrus occurring in thin sheets near the tropical tropopause with thicknesses between

* The National Center for Atmospheric Research is sponsored by the National Science Foundation.

Corresponding author address: Dr. Greg M. McFarquhar, NCAR/MMM, P.O. Box 3000, Boulder, CO 80307-3000.
E-mail: mcfarq@ncar.ucar.edu

a few hundred meters and one kilometer that were unusually horizontally homogeneous. A visible optical depth of 0.03 is used to distinguish subvisible cirrus clouds for this study, following the threshold derived by Sassen et al. (1989) using lidar and radiation flux measurements. It is emphasized that geometrically thin cirrus is not necessarily subvisible.

Although Sassen and Cho (1992) did detect subvisual cirrus using polarization lidar extended time observations in Salt Lake City, Utah, during the First International Satellite Cloud Climatology Project (ISCCP) Regional Experiment, and Sassen et al. (1998) observed a high cold cirrus cloud with an effective particle diameter of approximately 22 μm near Lamont, Oklahoma, the thin cirrus addressed here are primarily confined to the Tropics (Prabhakara et al. 1993; Winker and Trepte 1998). Because the thin cirrus were frequently observed 100–200 km away from the center of high-altitude cold-topped clouds, Prabhakara et al. (1988) inferred that they may be produced by the spreading of cirrus clouds, which are often present over convectively active areas such as the intertropical convergence zone and the Bay of Bengal. On the other hand, Heymsfield (1986) detected thin cirrus at the tropopause when convection was not active. Jensen et al. (1996) used a detailed cirrus cloud model to find two viable formation mechanisms: the transport of ice water to the tropopause by energetic tropical cumulonimbus clouds and slow, synoptic-scale uplift of layers.

Given the frequent occurrence of this cloud type and the importance of the warm pool region in the earth's radiative balance, it is crucial to quantify the effects of these clouds on outgoing longwave and incoming solar radiation and on the transport of water vapor into the stratosphere. Jensen et al. (1996) estimated that the absorption of infrared radiation results in heating rates on the order of a few degrees Kelvin per day, and Rosenfield et al. (1998), using an interactive chemistry–radiation–dynamics model, found that the increased radiative heating of 0.2–0.4 K day^{-1} from the clouds resulted in temperature increases of 2–4 K and vertical velocity increases of 0.05–0.1 mm s^{-1}. These warmer temperatures resulted in increases of 1 ppmv in the water vapor of the lower stratosphere. Prabhakara et al. (1993) also suggested that the greenhouse effect produced by these optically thin cirrus can be a significant factor in maintaining the warm pool.

Despite the considerable advances that have been made in aircraft instrumentation in recent years, there are still few good in situ measurements of these tropopause cirrus layers to test these modeling calculations on the effects of subvisible cirrus. To the best of our knowledge, data acquired in thin, nearly invisible tropopause cirrus layers by a WB-57 aircraft in the mid-1970s near Kwajalein, Marshall Islands (Heymsfield and Jahnsen 1974; Heymsfield 1986), and by the Aeromet Learjet in the same location in the early 1980s (Booker and Stickel 1982) are the only in situ measurements of subvisible tropopause cirrus. These data are revisited in order to estimate the heating rates that would be produced by these clouds. Heating rates are also calculated using optical depths estimated from the attenuated backscatter measurements acquired by the CLS during CEPEX and from those estimated from the SAGE II satellite data. Comparisons with some balloon-borne radiometer measurements are made. The relative importance of the two different formation mechanisms is estimated by examining ISCCP derived cloud properties for those times the SAGE II satellite detected subvisible cirrus. Implications for the radiative budget of the warm pool region are discussed.

2. In situ microphysical measurements and their radiative significance

a. In situ measurements

Tropopause cirrus layers were sampled near Kwajalein, Marshall Islands, using a high-altitude WB-57F high-altitude jet in the mid-1970s (Heymsfield and Jahnsen 1974; Heymsfield 1986). For the one case where original data are still available (18 December 1973), measurements were made between 16.2 and 16.7 km (temperatures of $-83°$ to $-84°$C). There was a double tropopause, one at 16.7 km and another weak tropopause between 16.2 and 16.5 km. The 0.5-km thickness is very close to the average thicknesses of other subvisible cirrus observed during this project and during CEPEX and TOGA COARE; the particle sizes were similar to those observed during four other cases (A. J. Heymsfield 1998, personal communication).

For measuring ice crystals, the WB-57F aircraft was equipped with a particle measuring system axially scattering spectrometer probe (ASSP), which sized in the range 2–30 μm, and a one-dimensional cloud (1DC) particle probe sizing in the range 20–300 μm. Excellent information about the crystal shape was obtained with a formvar replicator since the small crystals did not break up on impact. Heymsfield (1986) reported an approximately 50% mixture of trigonal plates and columns for the larger ice crystals measured by the replicator. Examples of the trigonal ice crystals observed are depicted in Figs. 3 and 4 of that paper, and of columnar ice crystals in Fig. 5. A bullet polycrystalline form and plate crystal are also depicted in Fig. 4.

Figure 1 of this paper shows the size distributions measured at six different altitudes in the cirrus using the ASSP data presented by Heymsfield and Jahnsen (1974). Crystals larger than 17 μm were not detected by the ASSP, and most were smaller than 10 μm. However, particles with maximum dimensions up to 50 μm were occasionally detected by the 1DC and are presented in Fig. 1 assuming that the crystals are evenly distributed over sizes up to the maximum crystal length detected. The ASSP did not detect the larger particles because its sample volume is very small. Gayet et al.

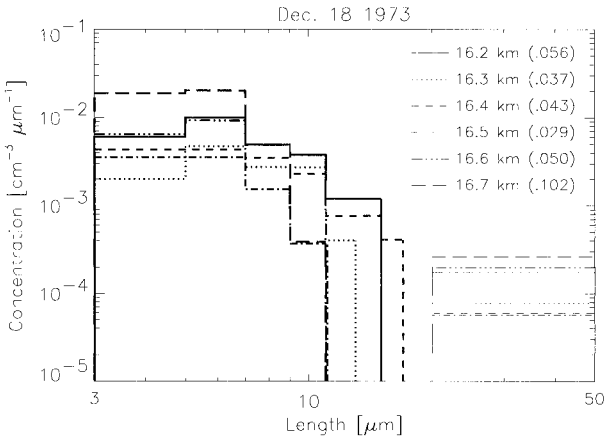

FIG. 1. Number size distributions at six altitudes during rapid descent by WB-57 aircraft through subvisual cirrus near Kwajalein, Marshall Islands, on 18 December 1973 (Heymsfield and Jahnsen 1974). Thick lines denote ASSP measurements, thin lines 1DC measurements. Total concentrations in cm^{-3} appear in parentheses after height.

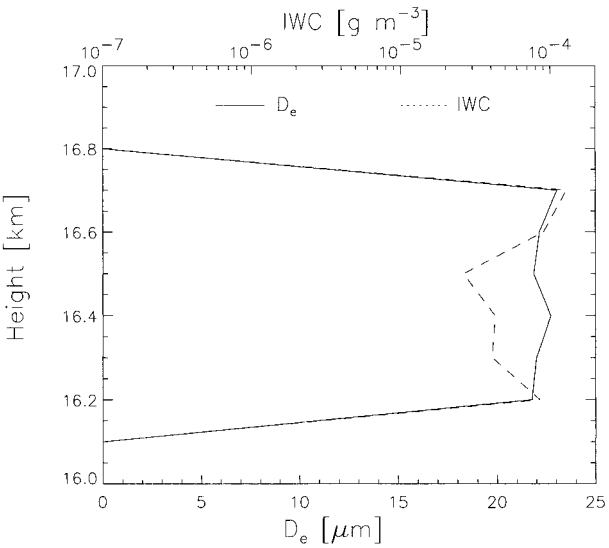

FIG. 2. Profile of IWC and D_e for subvisual cirrus depicted in Fig. 1.

(1996) found that the ASSP/forward scattering spectrometer probe–type probes give reliable measurements consistent with other probes in the presence of small quasi-spherical ice particles. Although the replicator only provides size information about the larger ice crystals, the smaller numbers of large crystals measured by the 1DC, in situ observations of quasi-circular small ice crystals during CEPEX (Heymsfield and McFarquhar 1996), and the reasonable overlap of the 1DC and ASSP observations suggests that the number distributions plotted in Fig. 1 from the ASSP are reasonable.

The 1DC is used to estimate particle mass by combining the replica shape information with the 1DC measurements. A profile of ice water content (IWC) calculated from the measured spectra using Heymsfield and Jahnsen's (1974) relationship between crystal length and crystal mass, is shown in Fig. 2. Both the contributions of small particles measured by the ASSP and the larger particles measured by the 1DC are included in the calculated profiles. While the ASSP measurements dominated the number concentrations, the 1DC measurements dominated the calculated mass. The double structure seen in Fig. 2, with a minimum in IWC at 16.5 km, was also observed with the mass densities estimated from the Stanford Research Institute ground-based lidar. Cirrus number densities derived from the lidar data agreed with the in situ densities within a factor of 2 when crystal information was considered (Uthe and Russell 1977).

The D_e [Fu and Liou (1993); Eq. (2.1)], is also shown in Fig. 2. There is no notable trend in altitude of typical particle sizes. The D_e are calculated using the Fu and Liou (1993) definition since their radiative code is used to calculate the radiative significance of this cloud; this definition assumes particles are hexagonal columns and represents the effective size as the mean-weighted crystal width. The visible optical depth, τ_{vis}, estimated from the microphysical data assuming Fu and Liou's (1993) relationship between mean effective size (D_e), IWC, and volume extinction coefficient (β_{ext}), is 0.007, greater than averages seen during CEPEX from lidar data (0.0045), but well within the range of typical values and below the visible threshold. Mass-weighted terminal velocities of 1–2 cm s^{-1} are estimated from the terminal velocities of the larger crystals (Heymsfield and Iaquinta 2000), corresponding to a descent of 1.7 km day^{-1}, suggesting that the presence of large-scale motions is needed to account for the ubiquitous nature of the subvisible cirrus.

Using the Aeromet Learjet, Booker and Stickel (1982) often noted a tenous cirrostratus in a thin and uniform layer just below the tropopause at Kwajalein, which was visible only at low sun angles or when flying above 10 km. On two occasions, the Learjet, instrumented with optical array particle measurement probes, was able to penetrate into and above the cloud layer. Figure 3 shows the IWC profile measured during a climb through the cirrus on 19 February 1981; a second tenuous layer 100 m thick at 15.4 km was not penetrated. From a rawinsonde sounding 6 h earlier, it is known that cloud temperature ranges from $-70°$ to $-80°$C. The IWCs and D_es are remarkably similar to those depicted in Fig. 2; the maximum crystal lengths were up to 140 μm. Booker and Stickel (1982) noted an intensification of the layer during the course of the measurements, and the cirrus was visible from the ground after this profile was obtained. They also stated that this was the most intense example of subvisible cirrus observed during the several years of their experiments, probably because it was the lowest and hence is not really an example of tropical tropopause cirrus. Although τ_{vis} is 0.012, almost double that of Heymsfield and Jahnsen (1974), it is still below

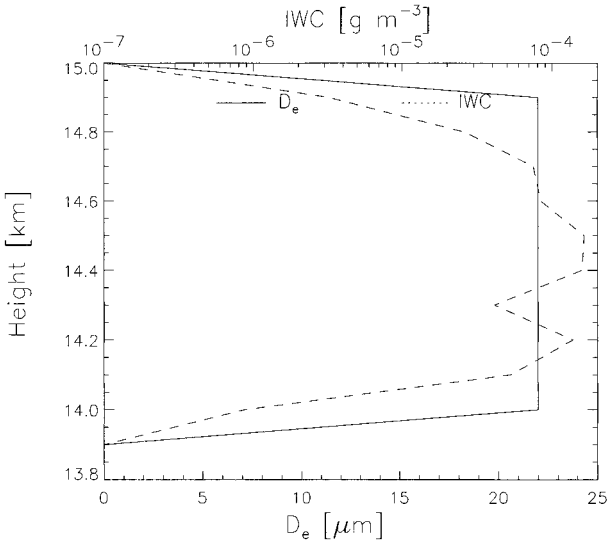

FIG. 3. Profile of IWC and D_e obtained in subvisual cirrus during ascent of Aeromet Learjet near Kwajalein, Marshall Islands, on 19 February 1981 (Booker and Stickel 1982).

the visible threshold. The D_e is constant because Booker and Stickel (1982) only presented one size distribution averaged over the 9 min of ascent. For the other case analyzed by Booker and Stickel (1982), they presented only one averaged particle size distribution for the entire ascent on 16 June 1978. For this 400-m-thick cloud with 15.5-km cloud top, this corresponds to an IWC of 1.5×10^{-5}, D_e of 7.9 μm, a τ_{vis} of 0.0036, and a maximum crystal size of approximately 30 μm.

b. Calculated radiative forcing

Fu and Liou's (1993) δ-four-stream approximation for radiative transfer was used to investigate the broadband solar and infrared radiative properties of these clouds. The Fu and Liou (1993) code parameterizes the basic single-scattering properties of ice crystals using third degree polynomials in terms of mean effective size; in the development of the parameterization the results were computed from a light scattering program including geometric ray tracing for size parameters larger than 30 and an exact spheroid solution for size parameters less than 30. The use of the four-stream code is necessary because two-stream codes cannot properly consider the scattering for thin cirrus, which may be highly peaked in the forward direction for the observed crystal shapes. The calculated radiative properties implicitly assume that the ice crystals with size parameters larger than 30 have a hexagonal shape, which is reasonable given the shapes observed by Heymsfield (1986). The IWC and D_e profiles are the required inputs to their code. In addition, the water vapor mixing ratio, ozone mixing ratio, and concentrations of CO_2, CH_4, and N_2O are based on the environmental tropical profile of Ellingson et al. (1991). A clear sky albedo of 0.1 for the ocean surface was used. The solar zenith angles were 42.9°, 58.0°, and 13.7° for the 17 December 1973, 19 February 1981, and 16 June 1978 cases respectively, with the last angle being estimated for local noontime since the times of the measurements were not available.

Within a cloud, ice saturation mixing ratio is assumed. This assumption is reasonable since the persistence of the cloud layers indicates that the particles must not be evaporating. In addition, during CEPEX a Lyman-α hygrometer measured humidities near the tropopause during dives made by the ER-2, for some cases, near 100%. Humidities were measured during a dive when the lidar saw cirrus immediately before and/or after the dive. However, the lidar did not provide useful data during the descent, so although the data are consistent, there is no way to prove that the high humidities were associated with cirrus (E. Weinstock 1998, personal communication).

Ackerman et al. (1988) found that the atmospheric heating rates produced by cirrus clouds were sensitive to the IWC, thickness, and environmental conditions. Here, we use the in situ measured properties to calculate the heating rates. Figure 4 shows the calculated net heating rates (infrared plus solar) for all three cases, compared to the clear sky heating rates. The clear sky heating rates are computed assuming saturation vapor pressure for the cloud location to more clearly see the effects of the cloud particles. For the Heymsfield and Jahnsen (1974) measurements, a maximum heating rate of 1.8 K day^{-1}, compared to the clear sky maximum of 0.4 K day^{-1}, is observed. The majority of the additional heating due to the clouds occurs in the infrared wavelengths. This corresponds to a net cloud radiative forcing of 0.8 W m^{-2}, 1.4 W m^{-2} in the infrared, and -0.6 W m^{-2} in the visible. For the two Booker and Stickel (1982) observed cases, maximum heating rates of 0.6–0.5 K day^{-1}, representing rates of 1.0–0.5 K day^{-1} greater than the clear sky values, are calculated. The corresponding cloud radiative forcings are 1.2 and 0.7 W m^{-2}, with 2.5 and 0.9 W m^{-2} in the infrared, and -1.3 and -0.2 W m^{-2} in solar channels.

The net radiative energy absorbed by subvisual cirrus results in a combination of local temperature change and induced upward vertical motion (Jensen et al. 1996). Assuming all of the absorbed energy results in the lifting of the cloud layer, for the observed potential temperature lapse rate of approximately 24 K km^{-1} (Heymsfield 1986) for the case in Fig. 4a, the layer potential temperature will increase at a rate of about 7 K day^{-1}, and the parcel will rise about 300 m in 1 day, or at a rate of 0.35 cm s^{-1}. A comparison of two soundings, the first made 24 h before the measurement period, suggested that the air in the cloud layer cooled by about 3°C, and assuming cooling along dry adiabats, this corresponds to an ascent rate of 0.7 cm s^{-1} (Heymsfield 1986), comparable to the calculated mass-weighted ter-

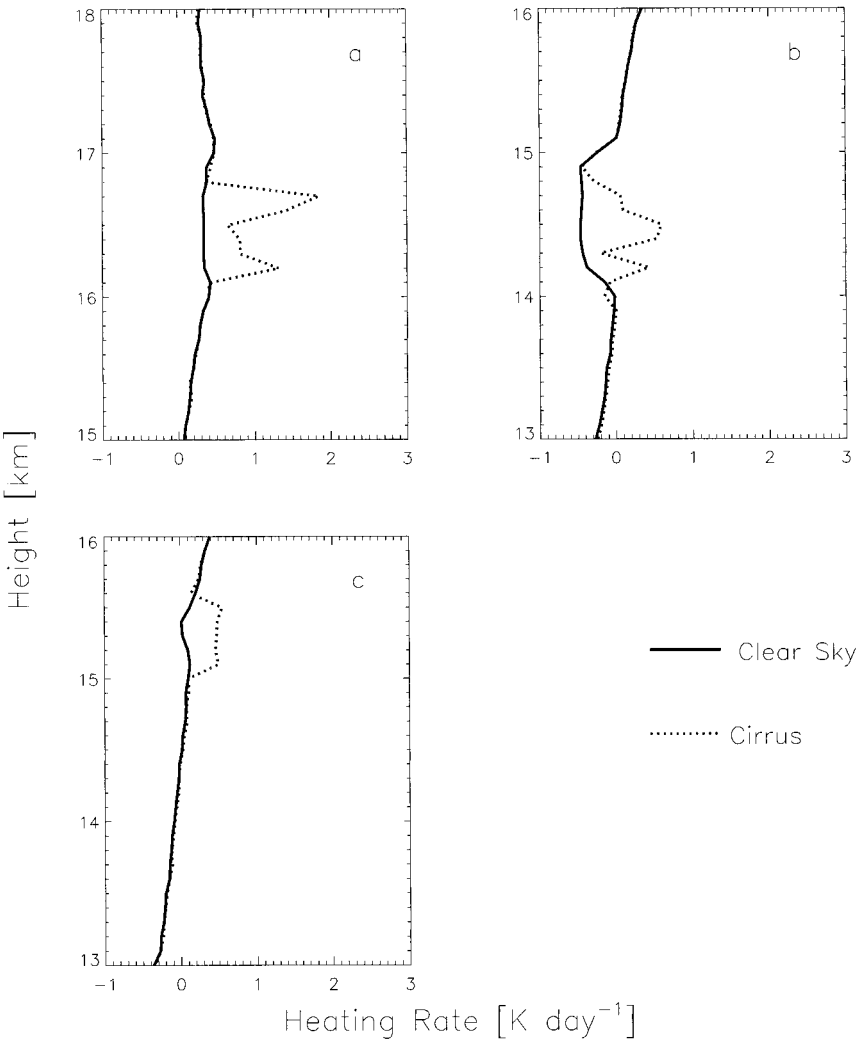

FIG. 4. Profiles of heating rate (dotted lines) derived from in situ microphysical measurements using Fu and Liou's (1993) δ-four-stream radiative transfer code for (a) 18 Dec 1973, (b) 19 Feb 1981, and (c) 16 Jun 1978. All measurements obtained near Kwajalein, Marshall Islands. Clear sky heating rates shown by solid lines (assume ice saturation within cloud).

minal velocities of 1–2 cm s^{-1}. Thus, it seems apparent that the large-scale dynamics should be considered in order to determine the influence of the absorbed energy. Rosenfield et al. (1998) also calculated similar radiative heatings to those calculated above and found that as a consequence water vapor increased in the lower stratosphere.

Jensen et al.'s (1996) maximum calculated heating rates are higher than those calculated for these three cases, on the order of 2 to 3 K day^{-1}, because their simulated optical depths, 0.028 and 0.023, are higher than those measured above. Because it is not known how representative these three cases of in situ cirrus measurements are, remote sensing measurements are used to derive a larger database of subvisible tropopause cirrus properties to further calculate their radiative impacts.

3. Lidar measurements and their radiative significance

a. Lidar measurements acquired during CEPEX and TOGA COARE

During CEPEX and TOGA COARE, the NASA ER-2 was equipped with the CLS, a nadir-pointing Nd:YAG lidar, which operated at wavelengths of 0.532 and 1.064 μm with a vertical resolution of 7.5 m (Spinhirne et al. 1982). Figure 5 shows cloud boundaries detected by the lidar for selected time periods during CEPEX and TOGA COARE. Tropopause cirrus were sometimes detected during time periods when no other clouds were present (Fig. 5a), during time periods when thick clouds were present below them (Fig. 5b), and when thin clouds were present below (Fig. 5c). Following Heymsfield and McFarquhar (1996), clouds are classified as thick when

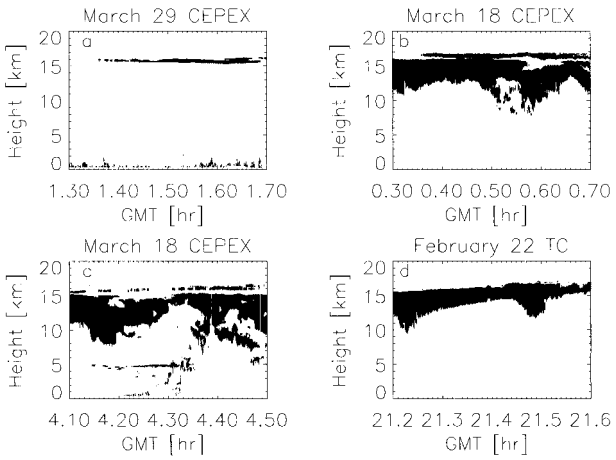

FIG. 5. (a), (b), and (c) represent examples of thin tropopause cirrus, following definition in text, obtained by Spinhirne's CLS lidar during CEPEX. Solid shading represents detected cloud layers. Ocean surface may be seen in (a) and (c). Profile in (d), obtained during TOGA COARE, does not represent thin tropopause cirrus because geometrically and optically thick cirrus layer extends to tropopause.

the lidar beam is occulted before reaching the ocean surface; this corresponds to an optical thickness of greater than 3 or 4 (Kinne et al. 1992).

Wang et al. (1994) noted that the majority of high clouds detected by SAGE II occurred within the top 2 km of the tropical troposphere. The CEPEX data were used to estimate the fractional occurrence of the tropopause cirrus, by identifying a cloud as tropopause cirrus provided that the top and bottom of the echo detected by the lidar occurred above 15 km; this height was chosen as being approximately 2 km below the typical height of the tropopause in the Tropics. The bottom of the cloud also must be above 15 km to prevent the inclusion of high thick anvils (e.g., see Fig. 5d). Manual checks against the lidar data for a number of time periods suggested that this definition seemed reasonable.

Tropopause cirrus were present 29% of the time during CEPEX and had a mean thickness of 0.47 km. Although CEPEX was fundamentally interested in validating the ''thermostat'' mechanism (Ramanathan and Collins 1991) and in determining how cirrus regulate the energy below clouds, the flight paths consisted of western and eastern triangular trajectories that typically did not deviate to sample specific clouds. Thus, although the samples are somewhat biased toward anvils, the data are more representative of the equatorial regions than that from TOGA COARE when convection was specifically targeted. A double cirrus layer was observed 13% of the time that the tropopause cirrus was present (e.g., Fig. 5a at 1.65 UTC). The mean thickness of the tropopause cirrus was 0.47 km, and on average the thickness of the cloud layer below the tropopause cirrus was 1.9 km. Thick cirrus below was present 43% of the time when the tropopause cirrus occurred, and clear sky (here defined as no cloud layers between 5 and 14 km) for 36% of the time. For time periods where thick cirrus were present (i.e., the lidar beam was occulted before reaching the ocean surface), tropopause cirrus was present 25% of the time, and for time periods where clouds were absent between 14 and 5 km (and the ocean surface was detected), tropopause cirrus were present 32% of the time. This shows that although the presence of tropopause cirrus can coincide with thicker anvils, there are also ample examples where the tropopause cirrus are at least somewhat removed, at least in the vertical, from convection or thicker anvils. The large-scale uplift for these cases could also be generated by flow over large-scale convective systems or their associated stratiform regions (Churchill and Houze 1990). Winker and Trepte (1998) also found these thin cirrus layers both in clear air and above intense tropical thunderstorms, and in regions characterized by large-scale subsidence in the midtroposphere.

The estimates above do not use the 0.03 threshold for defining subvisible cirrus because direct estimates of τ were not available for computing these statistics. Attempts to use Prabhakara et al.'s (1993) split-window method for estimating τ and D_e for cases during CEPEX when no cloud was underlying the thin tropopause cirrus failed because no signal could be detected in the 11.0- and 12.0-μm channels of the moderate resolution imaging spectrometer airborne simulator (D. Duda 1998, personal communication); the limit of detectability of the split-window method is closer to 0.05 or 0.1 optical depth.

On 29 March 1993 between 0124 and 0148 UTC (Fig. 5a), the NASA ER-2 overflew a thin cirrus with no cloud layers below. This case offers an excellent opportunity for estimating cloud heating rates and optical depths because there is no interference from cloud layers below and because the cloud layers are not complex in structure. The lidar-attenuated backscatter is converted to an effective optical depth, τ_{eff}, following Spinhirne et al.'s (1996) technique. Here, the effective ratio of backscatter to extinction cross section for the CLS signal is obtained by solving a system of linear equations and applying the lidar molecular and aerosol scattering under the cloud for a boundary condition. Here τ_{eff} underestimates the true optical depth because the effects of multiple scattering are not accounted for, but these effects may not be that significant given the low thicknesses and optical depths.

Figure 6 plots the variation of τ_{eff} over the flight track. The τ_{eff} values range from 0.0002 to 0.015, with a mean value of 0.0036, and encompass the range of values estimated for the three in situ cases. Even if the actual optical thickness is twice τ_{eff}, these clouds would still constitute subvisible cirrus. An increase in τ_{eff} to almost 0.015 around 0136 UTC is seen and seems to be related to the increase in geometric thickness and to the occurrence of a double cirrus layer at that time.

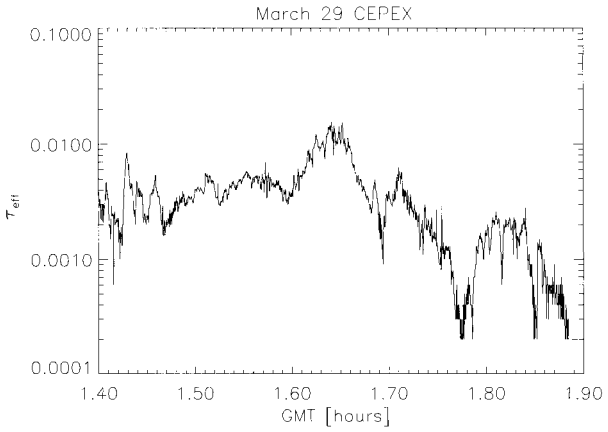

FIG. 6. Temporal variation of effective optical thickness, derived from CLS lidar measurements, for thin tropopause cirrus sampled on 0024 to 0154 UTC (GMT) 29 Mar 1993 during CEPEX at 2°S and 171°E.

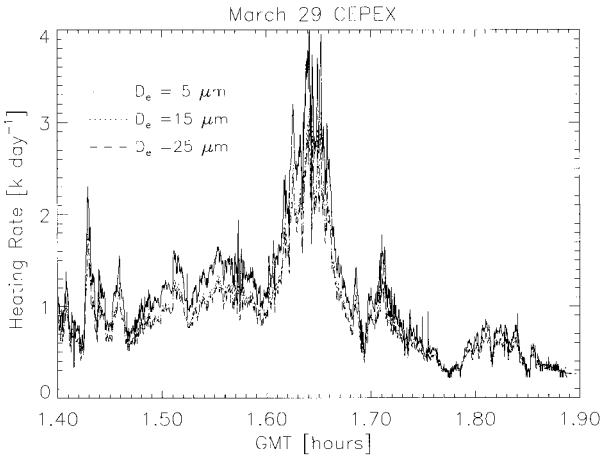

FIG. 7. Average heating rate, calculated using Fu and Liou's (1993) radiative transfer code, as a function of time for thin tropopause cirrus measured 0124 to 0154 UTC (GMT) 29 Mar during CEPEX. Solid, dotted, and dashed lines represent assumed D_e of 5, 15, and 25 μm, respectively.

b. Calculated radiative forcing

Figure 7 shows the average heating rate within the subvisible cirrus, assuming effective diameters from 5 to 25 μm, calculated with Fu and Liou's (1993) radiative transfer code. The D_e are chosen to encompass the range of sizes that would be expected based on the particle sizes that were observed during all the Kwajalein missions, not just those depicted in Fig. 2 and Fig. 3. An average cloud base and top, and average solar zenith angle between 124 and 154 UTC were selected for the computations. The heating rates follow the τ_{eff} trends depicted in Fig. 7, showing maximum values of almost 4 K day^{-1} when τ_{eff} exceeds 0.01 around 0138 UTC; the average heating rate is 1.1 K day^{-1} for the time period plotted. The heating rates drop to as low as 0.2 K day^{-1} when the observed τ_e drops to near 0.0001, essentially representing the clear-sky heating term (Fig. 4). The heating rates do not vary significantly for different D_e because τ, and not IWC, is held constant in the different simulations; there is some variation between simulations because of differences in the single-scattering properties. As for the simulations using the in situ microphysical data, the majority of the heating occurs in the infrared channels. At the time of maximum heating at 0138 UTC, of the 4.0 K day^{-1} heating, 79.7% occurs in the infrared.

The top of the atmosphere cloud radiative forcings (CRF) were also calculated from the simulation results, as shown in Fig. 8. At the time of maximum τ_{eff} and heating rate, the total CRF reached almost 2.5 W m^{-2}, of which 3.5 W m^{-2} was in the IR channels and -1 W m^{-2} in the solar channels. The averages for the time period plotted were 0.53, 0.77, and -0.24 W m^{-2}, respectively.

In order to get a more representative database of heating rates and optical depths for these cirrus clouds, the above analysis steps were repeated for the three other cases during CEPEX amenable to this type of analysis (15 March, 3 April, and 5 April); a simple cloud structure with no underlying cloud layers was observed for time periods during all of these days. Figure 9 shows a histogram of cloud optical depths obtained for these time periods. The average τ_{eff} for these time periods is 0.01. Despite efforts to filter out the occurrence of visible cirrus, the tail of the distribution at 0.1 indicates that some visible cirrus are included in the statistics.

Figures 10 and 11 show histograms of the average cloud heating rate and cloud radiative forcing, respectively. Appropriate solar zenith angles, cloud tops, and cloud bases were selected for each date. The heating rates and CRFs depended on both the physical location of the cloud and the solar zenith angle. The smallest

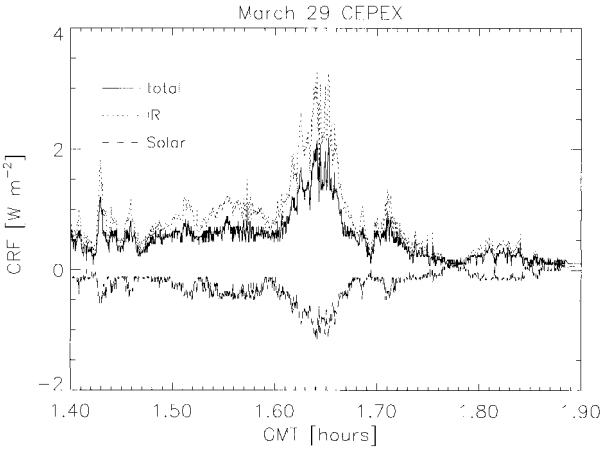

FIG. 8. Cloud radiative forcing, calculated using Fu and Liou's (1993) radiative transfer code, as a function of time for thin tropopause cirrus measured 0124 to 0154 UTC (GMT) 29 Mar during CEPEX. Solid, dotted, and dashed lines represent total CRF, CRF in infrared, and CRF in solar channels.

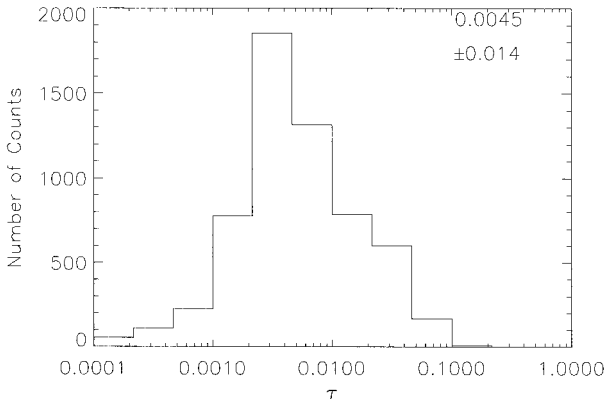

FIG. 9. Histogram of effective optical depth derived from CLS lidar measurements on NASA ER-2 for the following CEPEX cases: 16 Mar 0030 to 0112 UTC, 29 Mar 118 to 0200 UTC, 3 Apr 2030 to 2124 UTC, 5 Apr 2312 to 2336 UTC. Mean value and standard deviation for τ in upper right-hand corner.

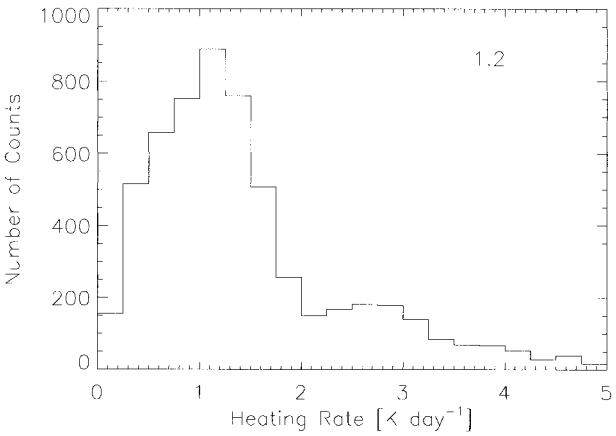

FIG. 10. Histogram of heating rates calculated for cases depicted in Fig. 9. Estimated solar zenith angles, geometric thicknesses, 5-μm effective diameter, and hexagonal column assumed for calculations. Median value of 1.2 K day^{-1} calculated.

possible D_e of 5 μm was used for these calculations, but the results are not highly sensitive to values of D_e between 5 and 25 μm. Of the average heating rate of 1.66 K day^{-1}, 1.29 K day^{-1} occurs in infrared channels, and 0.37 K day^{-1} in the solar channels. The CRF is similarly dominated by absorption of infrared radiation; for the average CRF of 1.58 W m^{-2}, 2.19 W m^{-2} is absorbed by the infrared, and 0.61 W m^{-2} is reflected by the solar channels.

There was necessarily some subjectivity in deciding what constituted thin tropopause cirrus since the analysis times for Figs. 9, 10, and 11 were chosen from the lidar cloud images before the effective optical depths were calculated. For example, on 3 April 1993 during CEPEX, the times between 2030 and 2124 UTC were included in the analysis, but time periods greater than 2124 UTC were not. Figure 12 shows the lidar-derived cloud boundaries for this case; for increasing time as the plane moves east along the 2°S latitude line, the cloud becomes geometrically and optically thicker. For example, at 2109 UTC the cloud has a thickness of 500 m and τ_{eff} of 0.0108; at 2121 UTC, 700 m and 0.0093; at 2136 UTC, 2.0 km and 0.0301; and at 2148 UTC, 3.0 km and 0.0886. This suggests that the cirrus should be visible from the ground at the later times. After 2120 UTC, the tropopause cirrus seemed to be attached to this larger cloud system, which was increasingly visible, and hence time periods corresponding to the entire attached cloud were excluded from the analysis.

Because of uncertainties in the cloud populations that are subvisible, it is desirable to calculate the maximum radiative effect that may be associated with these cirrus. Because heating rate and cloud radiative forcing are highly dependent on τ_{eff} for the δ-four stream calculations, assuming τ_{eff} equals 0.03 gives a good indication of this effect. Figure 13 shows the relationship between τ_{eff} and average cloud heating rate for all four CEPEX cases for which the CLS retrievals were performed. Each point represents a 5-s average along the flight track. Four distinct sample populations may be inferred that represent different solar zenith angles and cloud thicknesses assumed for the computations. For a τ_{eff} of 0.03, the heating rate ranges from less than 3 to 7 K day^{-1}, with the maximum heating rates occurring for the lower zenith angles. A similar plot for CRF (not shown) showed values of between 4 and 6 W m^{-2} for τ_{eff} of 0.03. Since $\tau > \tau_{\text{eff}}$, the the radiative effects of subvisible cirrus could be a bit larger. More scatter would be observed in the τ_{eff}–CRF–heating rate relationships if varying particle sizes and shapes were assumed.

The data used above still are limited to four cases during CEPEX. Hence, satellite data were used to develop a more representative climatology of the cirrus cloud properties.

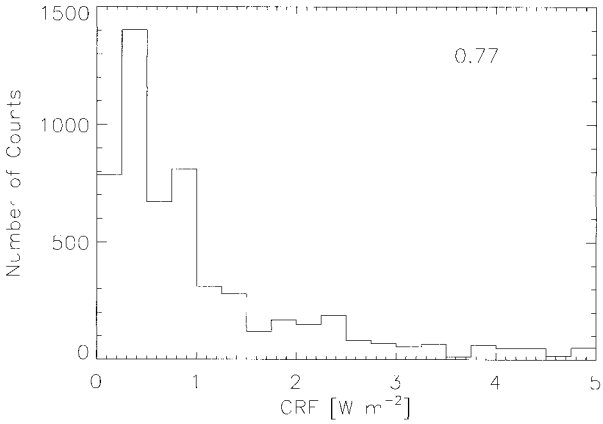

FIG. 11. Histogram of CRF calculated for cases depicted in Fig. 9. Calculations performed as for Fig. 10. Median value of 0.77 W m^{-2} calculated.

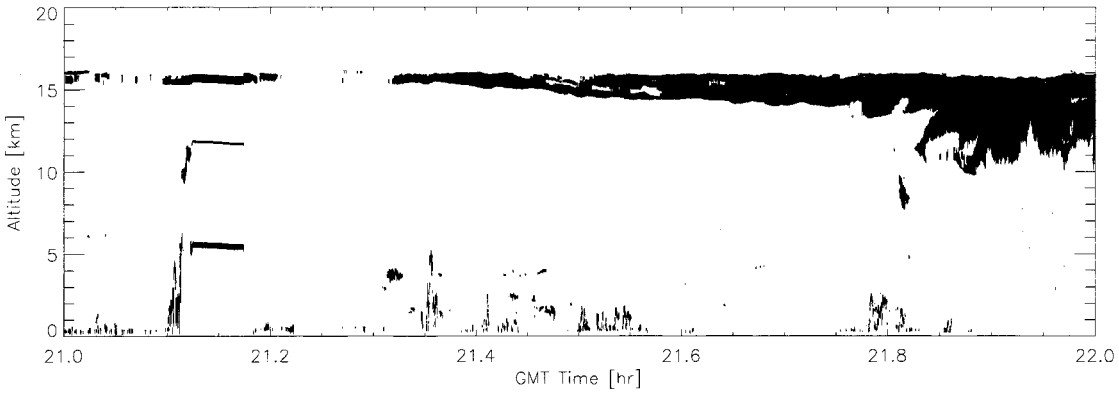

FIG. 12. Cloud boundaries detected by CLS on NASA ER-2, 2100–2200 UTC (GMT), 3 Apr 1993 during CEPEX.

4. Satellite occultation measurements

Satellite data have previously been used by Wang et al. (1996) and Prabhakara et al. (1993) to examine the properties of tropopause cirrus. As mentioned previously, the signal in the 10.8- and 12.6-μm bands, while useful for examining some examples of tropopause cirrus, are not able to detect tropopause cirrus that are subvisible. However, particle extinction measurements obtained from SAGE II are ideally suited for this purpose.

SAGE II data are sensitive to the presence of thin clouds because of the viewing geometry of the solar occultation technique that SAGE II uses; the profile of attenuated radiation is measured through the limb of the atmosphere at wavelengths between 0.385 and 1.02 μm during sunrise and sunset as encountered by the satellite. The viewing cross section is 0.5 km in the vertical and 2.5 km in the horizontal, and represent a pathlength of 200 km at 20-km height (Wang et al. 1994). The measurements are averaged to give 1-km vertical resolution. Because the beam is attenuated at an optical depth of 4, this means clouds with a maximum optical depth of 0.02 can be detected; the minimum optical depth is 2×10^{-6} because for smaller τ the contributions of the clouds are hidden by the Rayleigh extinction. In general, the extinction is underestimated by the SAGE satellite because uniform cloud coverage is assumed meaning that theoretically the derived extinction could represent the sampling of one dense bit of cirrus. However, given the persistent coverage and the relative uniformity of these clouds observed (e.g., Winker and Trepte 1998), it is not expected that this underestimate would be more than a factor of 2 for the homogeneous clouds at the tropical tropopause.

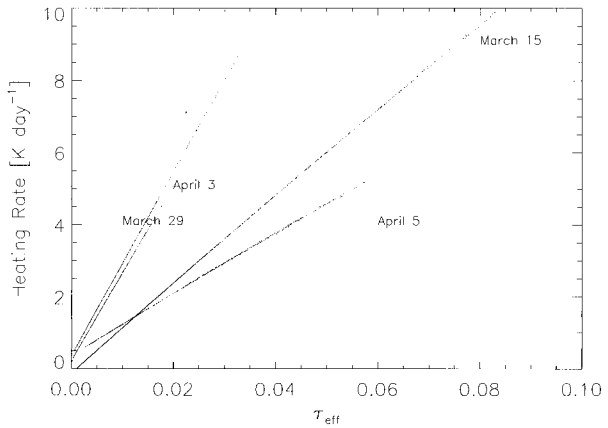

FIG. 13. The τ_{eff} vs heating rate calculated with Fu and Liou (1993) δ-four-stream code. Each point represents a 5-s average of the data. Different populations for different dates because of different solar zenith angles.

Following Wang et al. (1994), a cloud was assumed to occur whenever the ratio of the extinction at 0.525 μm to that at 1.02 μm was less than 2.1. The 1989 SAGE II data were used to develop a height-dependent climatology of cloud extinction coefficient because the years preceding that year were free of any major volcanic eruptions that would have complicated the analysis. Figure 14 shows height-dependent histograms of extinction coefficient calculated using the SAGE II data. To convert to optical depth, it is necessary to multiply by the thickness of the cloud; from the analysis presented in section 3, this thickness is estimated as 0.47 km, but Wang et al. (1996) obtained a much higher estimate of 2.6 km. It is likely that the lidar-based estimate is more representative of tropopause cirrus because it is based on finescale measurements, rather than coarsely averaged, 200-km satellite measurements. Further, Winker and Trepte (1998) also estimated thicknesses between a few hundred meters and one kilometer. The data presented in Fig. 14 are not filtered to exclude nontropical locations, but as Wang et al. (1996) point out, the occurrence of subvisible cirrus is limited almost exclusively to the Tropics, or between 20°N and 20°S. No significant changes occur when the extratropical data are removed.

The average optical depths in Fig. 14, around 0.001 to 0.004, are consistent with those derived from the lidar analysis in Fig. 9 and in the range of those observed

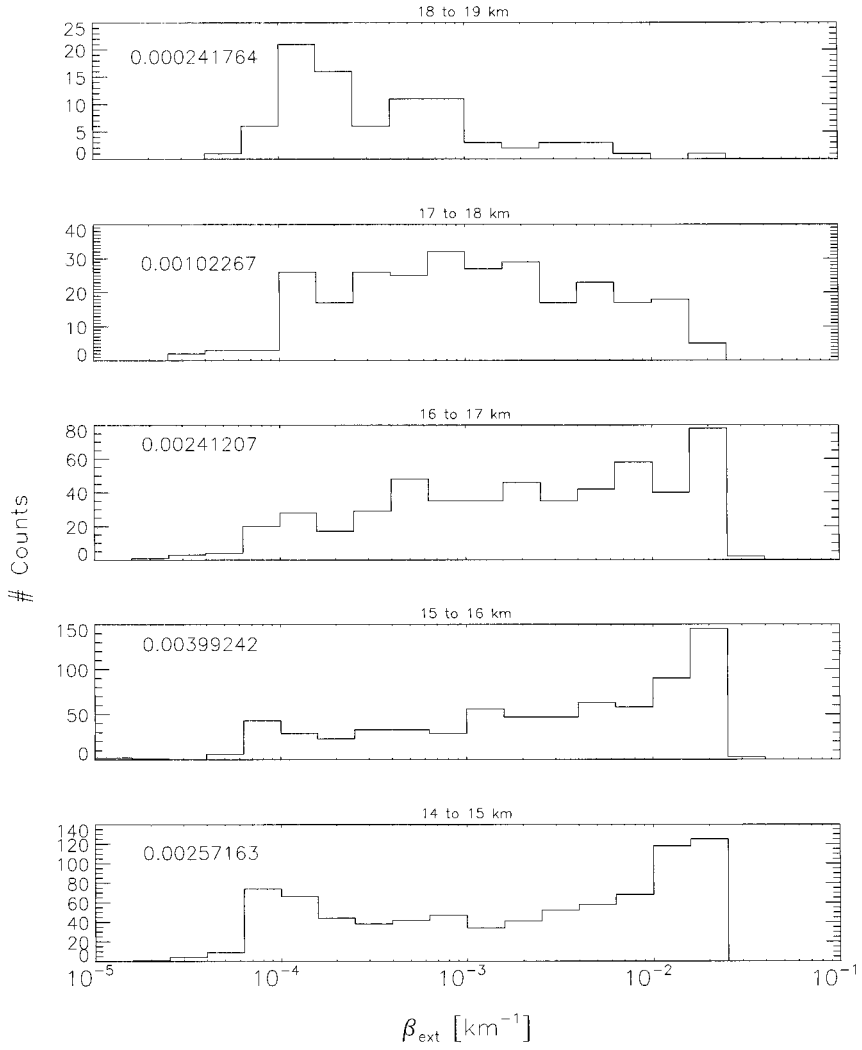

FIG. 14. Height-dependent histograms of number of occurrences of β_{ext} in ranges on horizontal axis obtained from SAGE II data for subvisible cirrus clouds using Wang et al. (1994) approach of defining subvisible cirrus clouds. Average β_{ext} for each height interval is listed.

by Nee et al. (1998) in Taiwan. As expected, the optical depths are larger for clouds at lower altitudes, probably due to a greater abundance of water vapor and particles. This suggests that our estimates for average heating rate of 1.3 K day^{-1} and CRF of 1.6 W m^{-2} are a reasonable representation for this cloud type. These estimates are also within the range of values quoted by the Jensen et al. (1996) and Rosenfield et al. (1998) modeling studies.

Nighttime measurements of infrared radiative heating, excluding effects of solar radiation, were made in the Tropics in the 1960s using balloon-borne net radiometer (Suomi and Kuhn 1958) with accuracies better than 2% (Bushnell and Suomi 1961). Although Bryson et al. (1963) found radiative warming rates greater than 30 K day^{-1} on one launch near India with no visible clouds, Darkow (1964) and Sandoval (1967) found persistent radiative heating in layers up to 100 mb below the tropopause, with values similar to those calculated above, for many launches made at four stations in the Caribbean (1.1 K day^{-1}), at Guam, Marinas Islands (between 1.3 and 2.6 K day^{-1}), and at Kanton Island (between 0.6 and 1.4 K day^{-1}). It cannot be determined whether these heating rates are due to subvisible cirrus since, with the exception of the Bryson et al. (1963) measurements, no coincident cloud observations were noted. But, given the persistent nature of the observed warming, and the ubiquitous nature of the subvisible cirrus, it seems that the two effects are at least somewhat related.

5. Discussion

Subvisible cirrus can be either generated in situ from larger-scale vertical motions or gravity waves, or they

can be remnants of anvils produced by deep convection. Clouds generated by both mechanisms have been observed. The three in situ cases reported here were not associated with convective activity. Heymsfield (1986) stated no clouds were observed with DMSP satellite measurements within a 480-km radius of the subvisible cirrus. This, combined with the 350-km horizontal extent and uniformity of the cloud strongly suggested it formed in situ. Booker and Stickel (1982) also observed that the cirrus observed 19 February 1981 did not advect into the area, but rather increased in intensity uniformly over a wide area around Kwajalein possibly as a result of a widespread lifting mechanism. The 16 June case existed 1 km above the highest convective cloud tops, as did some of the cirrus observed by Winker and Trepte (1998). They also noted that thin layers of cirrus occurred in regions characterized by large-scale subsidence in the midtroposphere and that their observation in the same region suggests cloud lifetimes can be on the order of days. In midlatitudes, Sassen et al. (1998) speculated that the homogeneous freezing of sulfuric acid droplets of stratospheric origin was the dominant ice-particle nucleation mode acting in the production of high, cold, corona-producing cirrus clouds.

However, some subvisible cirrus observed with the CLS system were detached from blow-off anvils associated with deep convection, such as that observed 3 April and depicted in Fig. 12. The Geostationary Meteorological Satellite imagery additionally showed intense cloud systems nearby (figure not shown). For other cases (e.g., 28 March), although no high cloud systems occurred nearby, minor amounts of high cloud occurred 24 h earlier, suggesting that these subvisible cirrus could be their remnants.

To estimate the relative contributions of subvisible cirrus produced by either mechanism, an attempt was made to determine the proximity of convective activity to the subvisible cirrus detected with SAGE II data. Given the times and locations of subvisible cirrus, ISCCP data were examined to determine if deep convection occurred within the approximately 2.5° by 2.5° grid box within which the subvisible cirrus were detected by the SAGE instrument. The Rossow and Schiffer (1991) ISCCP cloud classification scheme was used to identify deep convection, namely, deep convection occurs for pressures less than 310 mbar and optical depths greater than 22.63.

The analysis suggested that 27% (88 of 320 clouds) of the subvisible cirrus occurred in the vicinity of deep convection. The analysis was somewhat complicated by the fact that the limb-viewing technique meant that all subvisible cirrus measurements were made near sunrise or sunset. Because ISCCP requires daytime conditions to derive some cloud products, this means that cloud products were available for only 320 of 868 subvisible clouds. Because of this and because Danielsen (1982) noted from satellite observations that large cirrus anvils with areas greater than 200 km^2 and thicknesses of 1–3 km typically persisted for 5–10 h, more detailed analysis was performed to determine if any deep convection occurred in the grid box up to 12 h before the occurrence of the subvisible cirrus, ensuring that ISCCP products would be available for most instances of subvisible cirrus. It was determined that 38.7% (766 of 1982 clouds) of the subvisible cirrus occurred in areas where there had been some convective activity in the prior 12 h.

Prabhakara et al. (1988), using IRIS data, had previously deduced that thin cirrus clouds were 100–200 km away from the center of high-altitude cold clouds, and hence were associated with convectively active regions. However, the thin cirrus that they studied are not necessarily the same as the subvisible cirrus studied here, since these subvisible cirrus are not dense enough to detect with their split-window technique. This shows the difference in terminology between subvisible cirrus and thin cirrus: the thin cirrus are more apt to be detached from the deep convection. The analysis presented here shows that consideration must be given to both formation mechanisms, as both seem to occur with reasonable frequencies in the Tropics.

Finally, the calculations of heating rate and CRF may be used to determine if subvisible cirrus are climatically significant. Prabhakara et al. (1993) inferred that the greenhouse effect produced by the optically thin cirrus clouds could be a significant factor in maintaining the warm pool, since they pervasively occurred in this region of local maximum in net input of radiative energy. However, the subvisible cirrus sampled here are a subset of their thin cirrus, and are optically thinner and hence less radiatively significant. Here, the average cloud radiative forcing is estimated as 0.7 W m^{-2}, but values as high as 4–5 W m^{-2} can occur for subvisible cirrus. Using Hartmann et al.'s (1992) Earth Radiation Budget dataset, Heymsfield et al. (1998) indicated that ''thin'' cirrus absorbed 11 W m^{-2} of longwave radiation and reflected 6 W m^{-2} of shortwave radiation in the Tropics. Their ''thin''–''thick'' cirrus separation occurred at an albedo of 0.40, which corresponds to τ much greater than for the subvisible cirrus treated here. For comparison, they calculated the column-integrated radiative forcing (longwave minus shortwave) produced by thick tropical cirrus as approximately -9 W m^{-2} for a zonally averaged latitude band 22° wide centered on the equator.

This suggests that although the effect of subvisible cirrus on the radiative budget is not as significant as for other types of ice clouds, their contributions on the radiative budget of the warm pool region can still be significant and should not be ignored. Subvisible cirrus also affect upper-troposphere vertical motions, and hence they should be properly accounted for to obtain an accurate picture of heat and energy balance. Further, the calculated heating rates are within the ranges of values calculated by the modeling studies of Jensen et al. (1996) and Rosenfield et al. (1998), who showed that such heating and induced motions can be important for the lower-stratospheric water vapor budget.

6. Conclusions

By using in situ microphysical and lidar observations of subvisible tropopause cirrus as input to a δ-four-stream radiative transfer model, solar and infrared heating rates, and cloud radiative forcings were calculated. Retrievals of extinction coefficients from the SAGE II satellite supplemented these calculations. The calculated heating rates and CRFs mainly depend on the observed optical thickness of the cloud layers, and to a lesser extent, the effective particle size and geometric thickness. The principal findings of this study are summarized below.

1) Using the lidar data during CEPEX and TOGA COARE, it was estimated that cirrus with geometric thicknesses less than 2 km and mean geometric thicknesses of 0.47 km occur near the tropopause approximately 29% of the time. Thick cirrus with τ greater than 3 or 4 were present for 43% of these times, and clear sky was below the thin cirrus for 36% of these times.
2) In situ microphysical measurements in subvisible cirrus clouds suggest typical IWCs between 10^{-6} and 10^{-4} g m^{-3}, D_es between 5 and 25 μm, and maximum crystal sizes between 30 and 140 μm.
3) Heating rates calculated from a δ-four-stream radiative transfer code (Fu and Liou 1993) using the microphysical and lidar data during CEPEX, assuming the cloud was composed of hexagonal crystals, suggested that the heating rates ranged from nearly 0 to 6 K day^{-1}, with an average of 1.66 K day^{-1}. Approximately 80% of this heating occurred at infrared wavelengths.
4) Cloud radiative forcings (CRFs) calculated from the same code averaged 1.58 W m^{-2}, with values as high as 5 W m^{-2} for some subvisible cirrus. For the average 1.58 W m^{-2}, 2.19 W m^{-2} occurred in the infrared and -0.61 W m^{-2} at solar wavelengths.
5) There are two viable formation mechanisms, deep convection and formation in situ, and examples of both have been noted in the Tropics. By comparing the SAGE II data with ISCCP-derived cloud properties, it was estimated that between 27.5% and 37.8% of subvisible cirrus detected by SAGE II during 1989 occurred in the vicinity of deep convection.
6) A careful distinction must be made between thin cirrus and subvisible cirrus when assessing radiative characteristics. The Sassen et al. (1989) definition should be used to distinguish the properties of subvisible cirrus. However, the two types are closely related for cirrus produced by deep convection.
7) Compared to other cloud types in the Tropics, the cloud radiative forcings and heating rates are not as large, but large enough to be radiatively important given the delicate balance between short-wave cooling and long-wave heating in this region. Effects of subvisible cirrus on vertical motions and circulations and on the water budget of the stratosphere are equally important.

The in situ measurements used in this study still come from a limited sample. With recent advances in aircraft instrumentation, substantial improvements could be made in the database of sizes and shapes of small crystals in these clouds, allowing a more accurate radiative transfer calculation that can take into account the different sizes and shapes of ice crystals.

Acknowledgments. The support of the NSF Climate Dynamics Program, NSF Award ATM-9640613 and of the Center for Clouds, Chemistry and Climate (C^4) at the Scripps Institution of Oceanography is acknowledged. We appreciate the use of the δ-four stream code from Qiang Fu of Dalhousie University. We are also grateful for the assistance provided by Nicholas Nali of the University of Wisconsin, by P.-H. Wang of the Science and Technology Corporation, David Duda of NASA Goddard, and Elliot Weinstock of Harvard University. The SAGE II and ISCCP data were obtained from the NASA Langley Research Center EOSDIS Distributed Active Archive Center. We appreciate the thoughtful reviews of W. Collins, S. Aulenbach, W. Grabowski, D. Mitchell, and an anonymous reviewer.

REFERENCES

Ackerman, T. P., K. N. Liou, F. P. J. Valero, and L. Pfister, 1988: Heating rates in tropical anvils. *J. Atmos. Sci.,* **45,** 1606–1623.

Booker, D. R., and P. G. Stickel, 1982: High altitude tropical cirrus cloud observations. Preprints, *Conf. on Cloud Physics,* Chicago, IL, Amer. Meteor. Soc., 215–217.

Bryson, R. A., C. A. Wilson III, and P. M. Kuhn, 1963: Some preliminary results from radiation sonde ascents over India. *Proc. WMO–IUGG Symp. Tropical Meteorology,* Rotorua, New Zealand, WMO–IUGG, 507–516.

Bushnell, R. H., and V. E. Suomi, 1961: Experimental flight verification of the economical net radiometer. *J. Geophys. Res.,* **66,** 2843–2848.

Churchill, D. D., and R. A. Houze Jr., 1990: Radiatively driven stratosphere–troposphere interactions near the tops of tropical cloud clusters. Preprints, *Conf. on Cloud Physics,* San Francisco, CA, Amer. Meteor. Soc., J125–J128.

Danielsen, E. F., 1982: A dehydration mechanism for the stratosphere. *Geophys. Res. Lett.,* **9,** 605–608.

Darkow, G. L., 1964: A study of infrared radiation measurements in the vicinity of the subtropical tropopause. Ph.D. thesis, University of Wisconsin, 67 pp. [Available from University of Wisconsin Library, B106B Library, 728 State St., Madison, WI 53706.]

Ellingson, R. G., J. Ellis, and S. Fels, 1991: The intercomparison of radiation codes used in climate models: Long wave results. *J. Geophys. Res.,* **96,** 8929–8953.

Fu, Q., and K. N. Liou, 1993: Parameterization of the radiative properties of cirrus clouds. *J. Atmos. Sci.,* **50,** 2008–2025.

Gayet, J.-F., G. Febvre, and H. Larsen, 1996: The reliability of the PMS FSSP in the presence of small ice crystals. *J. Atmos. Oceanic Technol.,* **13,** 1300–1310.

Hartmann, D. L., M. E. Ockert-Bell, and M. L. Michelsen, 1992: The effect of cloud type on earth's energy balance: Global analysis. *J. Climate,* **5,** 1281–1304.

Heymsfield, A. J., 1986: Ice particles observed in a cirriform cloud

at −83°C and implications for polar stratospheric clouds. *J. Atmos. Sci.,* **43,** 851–855.
——, and L. J. Jahnsen, 1974: Microstructure of tropopause cirrus layers. *Proc. Sixth Conf. on Aerospace and Aeronautical Meteorology,* El Paso, TX, Amer. Meteor. Soc., 43–48.
——, and G. M. McFarquhar, 1996: High albedos of cirrus in the tropical Pacific warm pool: Microphysical interpretations from CEPEX and from Kwajalein, Marshall Islands. *J. Atmos. Sci*., **53,** 2424–2451.
——, and J. Iaquinta, 2000: Cirrus crystal terminal velocities. *J. Atmos. Sci.,* **57,** 914–936.
——, G. M. McFarquhar, W. D. Collins, J. A. Goldstein, F. P. J. Valero, J. Spinhirne, W. Hart, and P. Pilewskie, 1998: Cloud properties leading to highly reflective tropical cirrus: Interpretations from CEPEX, TOGA COARE, and Kwajalein, Marshall Islands. *J. Geophys. Res.,* **103,** 8805–8812.
Jensen, E. J., O. B. Toon, H. B. Selkirk, J. D. Spinhirne, and M. R. Schoeberl, 1996: On the formation and persistence of subvisible cirrus clouds near the tropical tropopause. *J. Geophys. Res.*, **101,** 21 361–21 375.
Kinne, S., T. P. Ackerman, A. J. Heymsfield, F. P. J. Valero, K. Sassen, and J. D. Spinhirne, 1992: Cirrus microphysics and radiative transfer: Cloud field study on 28 October 1986. *Mon. Wea. Rev.*, **120,** 661–685.
Nee, J. B., C. N. Len, W. N. Chen, and C. I. Lin, 1998: Lidar observation of the cirrus cloud in the tropopause at Chung-Li (25°N, 121°E). *J. Atmos. Sci.,* **55,** 2249–2257.
Platt, C. M. R., S. A. Young, P. J. Manson, G. R. Patterson, S. C. Marsden, and R. T. Austin, 1998: The optical properties of equatorial cirrus from observations in the ARM pilot radiation observation experiment. *J. Atmos. Sci.,* **55,** 1977–1996.
Prabhakara, C., R. S. Fraser, G. Dalu, M.-L. C. Wu, and R. J. Curran, 1988: Thin cirrus clouds: Seasonal distribution over oceans deduced from Nimbus-4 IRIS. *J. Appl. Meteor.,* **27,** 379–399.
——, D. P. Kratz, J.-M. Yoo, G. Dalu, and A. Vernekar, 1993: Optically thin cirrus clouds: Radiative impact on the warm pool. *J. Quant. Spectrosc. Radiat. Transfer,* **49,** 467–483.
Ramanathan, V., and W. Collins, 1991: Thermodynamic regulation of ocean warming by cirrus clouds deduced from observations of 1987 El Nino. *Nature*, **351,** 27–32.
Rosenfield, J. E., D. B. Considine, M. R. Schoeberl, and E. V. Browell, 1998: The impact of subvisible cirrus clouds near the tropical tropopause on stratospheric water vapor. *Geophys. Res. Lett.,* **25,** 1883–1886.
Rossow, W. B., and R. A. Schiffer, 1991: ISCCP cloud data products. *Bull. Amer. Meteor. Soc.,* **72,** 2–20.
Sandoval, A. R., 1967: Background studies for a climatology of the intertropical convergence zone in the Western Central Pacific Area. Ph.D. thesis, University of Wisconsin, 97 pp. [Available from University of Wisconsin Library, B106B Library, 728 State St., Madison, WI 53706.]
Sassen, K., and B. S. Cho, 1992: Subvisual-thin cirrus lidar dataset for satellite verification and climatological research. *J. Appl. Meteor.,* **31,** 1275–1285.
——, M. K. Griffin, and G. C. Dodd, 1989: Optical scattering and microphysical properties of subvisible cirrus clouds, and climatic implications. *J. Appl. Meteor.,* **28,** 91–98.
——, G. G. Mace, J. Hallett, and M. R. Poellot, 1998: Corona-producing ice clouds: A case study of a cold mid-latitude cirrus layer. *Appl. Opt.,* **37,** 1477–1485.
Spinhirne, J. D., M. Z. Hansen, and L. O. Caudill, 1982: Cloud top remote sensing by airborne lidar. *Appl. Opt.,* **22,** 1564–1571.
——, W. D. Hart, and D. L. Hlavka, 1996: Cirrus infrared parameters and shortwave reflectance relations from observations. *J. Atmos. Sci.,* **53,** 1438–1458.
Suomi, V. E., and P. M. Kuhn, 1958: An economical net radiometer. *Tellus,* **10,** 160–163.
Uthe, E. E., and P. B. Russell, 1977: Lidar observations of tropical high-altitude cirrus clouds. *Radiation in the Atmosphere,* H. J. Bolle, Ed., Science Press, 242–244.
Wang, P.-H., M. P. McCormick, L. R. Poole, W. P. Chu, G. K. Yue, G. S. Kent, and K. M. Skeens, 1994: Tropical high cloud characteristics derived from SAGE II extinction measurements. *Atmos. Res.,* **34,** 53–83.
——, ——, P. Minnis, G. S. Kent, G. K. Yue, and K. M. Skeens, 1996: Preliminary results of the vertical structure of Tropical (20°S–29°N) subvisual clouds from SAGE II observations. *Proc. 12th Int. Conf. on Cloud and Precipitation,* Zurich, Switzerand, International Commission on Clouds and Precipitation, 637–640.
Winker, D. M., and C. R. Trepte, 1998: Laminar cirrus observed near the tropical tropopause by LITE. *Geophys. Res. Lett.,* **25,** 3351–3354.